Earth and Planetary Science Letters 271 (2008) 348–358

Contents lists available at ScienceDirect

Earth and Planetary Science Letters

journal homepage: www.elsevier.com/locate/epsl

Lateral variations in CMB heat flux and deep mantle seismic velocity caused by a thermal–chemical-phase boundary layer in 3D spherical convection

Takashi Nakagawa [a,*], Paul J. Tackley [b]

[a] Department of Earth and Planetary Sciences, Kyushu University, Fukuoka, Japan
[b] Institute of Geophysics, ETH Zurich, Switzerland

ARTICLE INFO

Article history:
Received 27 August 2007
Received in revised form 27 February 2008
Accepted 11 April 2008
Available online 23 April 2008

Editor: C.P. Jaupart

Keywords:
thermo-chemical mantle convection
3D spherical shell
CMB heat flow
seismic anomalies
lateral heterogeneities

ABSTRACT

Numerical simulations of thermo-chemical, multi-phase, compressible mantle convection in a three-dimensional spherical shell are used to investigate the relationship between lateral variations in seismic shear-wave velocity V_s above the core–mantle boundary (CMB) and lateral variations in heat flux across the CMB (q_{CMB}), when compositional variations and the post-perovskite phase transition are included. For simple thermal convection, the V_s–q_{CMB} relationship is reasonably but not perfectly linear. The post-perovskite transition introduces a non-linearity that amplifies fast V_s anomalies in cold regions, but there is still a unique mapping between δV_s and q_{CMB}. Lateral variations in composition such as piles of dense material introduce another non-linearity that affects hot upwelling regions, and introduces a non-uniqueness in δV_s–q_{CMB} if the dense material (e.g., MORB) is seismically fast compared to the surrounding material. In this case, dense piles are ringed by sharp, low-V_s anomalies. If the CMB is covered by a global dense layer than variations in δV_s and q_{CMB} are reduced but so is the mean value of q_{CMB}. In all cases, the peak-to-peak lateral variation in q_{CMB} is similar to or larger than twice the mean value, which might create problems for generating a dynamo according to existing numerical dynamo simulations. Analytical scalings are developed to explain the observed trends.

1. Introduction

Mantle convection controls the mean heat flux, and the spatial variation of heat flux, across the core–mantle boundary. Core–mantle thermal coupling processes have been proposed in various geomagnetic studies as an explanation for why the observed magnetic field (both present-day and over the last few centuries) is not completely symmetric like an axial dipole (e.g., Bloxham and Gubbins, 1987), as an explanation for the particular secular variation that is observed (e.g., Bloxham, 2000b), as an explanation for the large variation in reversal rate in the geological record (e.g., Larson and Olson, 1991), and as an explanation for the preferred path of the dipole during reversals (Clement, 1991; Laj et al., 1991; Love, 2000; Costin and Buffett, 2004). Several numerical magnetoconvection or geodynamo simulations have been performed with heterogeneous heat flux at the core–mantle boundary in order to understand the effect of this thermal coupling (Glatzmaier et al., 1999; Bloxham 2000a,b; Olson and Christensen, 2002; Christensen and Olson, 2003; Aubert et al., 2007). However, it is not clear what is the most realistic boundary condition for such numerical geodynamo models, in terms of the variation of heat flux and the its relationship to seismic tomography in the deepest mantle.

The usual approach to estimating the spatial variations in heat flux across the CMB is to linearly scale the spatial patterns of seismic tomography in the core–mantle boundary region. Thus is obtained a non-uniform heat flux boundary condition for geodynamo simulations (Glatzmaier et al., 1999; Olson and Glatzmaier, 1996; Olson and Christensen, 2002; Christensen and Olson, 2003):

$$\delta q_{CMB}(\theta,\varphi) = C\delta V_s(r = r_{CMB},\theta,\varphi) \quad (1)$$

where the scaling factor C [W/m^2] was estimated from isochemical and isoviscous mantle convection models in a spherical shell (e.g. Olson and Glatzmaier, 1996). These results have indicated that thermal coupling between the mantle and the core induced by this non-uniform heat flux is the strongest mechanism for inducing non-dipolar fields produced by the geodynamo, as well as strongly influencing the reversal frequency and the secular variation. In these studies, the scaling factor C was assumed to be a constant, which means that the seismic anomalies in the CMB region are directly proportional to the lateral variation of CMB heat flux. The above geodynamo models also indicated that when the lateral variation in heat flux is too large, the dynamo process may not operate.

Recent work on the structure, composition and dynamics of the CMB region has indicated that both variations in composition (e.g., Trampert et al., 2001; Deschamps et al., 2007; Ritsema et al., 2007) and the existence of the post-perovskite (PPV) phase transition (e.g., Murakami et al., 2004; Tsuchiya et al., 2004; Oganov and Ono,

* Corresponding author. Tel.: +81 92 642 2313; fax: +81 92 642 2684.
E-mail address: takashi@geo.kyushu-u.ac.jp (T. Nakagawa).

0012-821X/$ – see front matter © 2008 Elsevier B.V. All rights reserved.
doi:10.1016/j.epsl.2008.04.013

Table 1
Model physical mantle parameters

Symbol	Meaning	Non-D. value	Dimensional value
η_0	Reference viscosity	1	1.27×10^{22}
ρ_0	Reference (surface) density	1	3300 kg m^{-3}
g	Gravity	1	9.8 m s^{-2}
α_0	Ref. (surface) thermal expan.	1	5×10^{-5} K^{-1}
κ_0	Ref. (surface) thermal diff.	1	7.656×10^{-7} m^{2}s^{-1}
ΔT_{sa}	Temperature scale	1	2500 K
T_s	Surface Temperature	0.12	300 K
R_H	Radioactive heating	15.75	4.2×10^{-12} Wkg^{-1}
C_p	Heat capacity	1	1250 JK^{-1}
d	Thickness of mantle	1	2890 km
Ra_0	Rayleigh number	10^7	N/A
Di_0	Surface dissipation number	1.13	N/A
<Di>	Mean dissipation number	0.439	N/A
ρ_{CMB}	CMB density	1.7567	5797 kg m^{-3}
α_{CMB}	CMB thermal expan.	0.1729	0.8645×10^{-5} K^{-1}
κ_{CMB}	CMB thermal diff.	3.093	2.368×10^{-6} m^{2}m^2 s^{-1}

$Ra_0=\rho_0 g\alpha_0\Delta T_{sa}d^3/\kappa_0\eta_0$ and $Di=\alpha_0 gd/C_p$. For radioactive heating, the value is averaged over total volume of mantle because dense basaltic material is enhanced by 10 times relative to harzburgite material.

2004) are necessary to explain the observed heterogeneous structures in the CMB region (e.g., Lay et al., 2006). Geodynamic convection modeling (Nakagawa and Tackley, 2005, 2006) confirmed that both factors are important in obtaining large-scale and strong heterogeneities in the lowermost mantle.

Thus, the CMB region is probably rather complex, with variations in composition and phase (perovskite to PPV) in additional to thermal variations, whereas the above scaling law has so far only found to be applicable to simple isothermal, isoviscous convection. Two questions arise: (1) Is a linear scaling really appropriate for this thermo-chemical-phase boundary layer? (2) How large are the lateral variations in CMB heat flow in such a more realistic situation?

In the models of (Nakagawa and Tackley, 2005, 2006), the geometry of the mantle was assumed to be a two-dimensional cylindrical shell or three-dimensional rectangular box. In the more realistic three-dimensional spherical shell geometry, several works have studied the behavior of compositional layering above the CMB (McNamara and Zhong, 2004; McNamara and Zhong, 2005; Oldham and Davies, 2004), but these focused on the morphology of layering, not lateral variations of the CMB heat flux, and did not include the post-perovskite phase transition.

In order to study the scaling relationship between lateral variations of CMB heat flux and seismic anomalies in a combined thermal–chemical-phase CMB region (as is useful for numerical geodynamo models with a heterogeneous boundary condition), we here present numerical simulations of thermo-chemical, multiphase and compressible mantle convection in a three-dimensional spherical shell. These simulations produce more realistic scenarios for CMB heterogeneity than those previously used to study this scaling, including thermal–chemical-phase structures and the influence of variable viscosity (temperature- and depth-dependent viscosity but for simplicity, not plate-like). We analyze the relationship between CMB heat flow and seismic velocity, including the amplitude of lateral variation of CMB heat flow and discuss its possible influence on the geodynamo.

2. Model description

The physical model adopted is similar to that in previous studies (e.g., Nakagawa and Tackley, 2005, 2006), using the infinite Prandtl number, compressible anelastic equations with temperature- and depth-dependent viscosity, compositional variations and multiple phase transitions including perovskite to post-perovskite. Solution in a 3-D spherical shell is obtained using an upgraded version of the numerical code STAG3D, which originally modelled a 3-D cartesian box (Tackley, 1993, 1996). Spherical shell geometry was implemented using the 'Yin–Yang' grid (Kageyama and Sato, 2004; Kageyama, 2005), in which two (longitude, latitude, radius) subgrids of size ±45 ° in latitude and 270° in longitude are meshed together to make a complete sphere, rather like the construction of a tennis ball, and thereby avoiding the "pole problem" while still retaining the advantages of an orthogonal grid. The numerical procedures and features of the original rectangular version (Tackley, 1998) are carried over to the Yin–Yang version, with documentation and benchmarking presented in (Tackley, submitted to PEPI), where it is shown that the code generates the same results for steady-state basally-heated convection as results from 8 other codes compiled by (Stemmer et al., 2006), and for compressible, phase-change modulated convection generates similar results to those that (Tackley et al., 1993) obtained using a spectral code.

The viscosity is given by

$$\eta = \eta_0(1+29H(0.7716-z))\exp(4.6(1-z))\exp\left(\frac{13.815}{T+0.88}\right) \quad (2)$$

where H is Heavyside step function to express the viscosity jump at 660 km depth and η_0 is the reference viscosity at $T=1$ (2500 K) and $z=0$. So, the viscosity changes by three orders of magnitude with temperature between 300 K (non-dimensional 0.12) and 2800 K (non-dimensional 1.12) and two orders for depth, plus a jump of factor 30 at the upper-lower mantle interface. The numerical resolution is $64\times192\times64\times2$ (equivalent to 256(lon)×128 (lat)×64 (rad) for a global grid) with an average of 16 tracers per cell to track the compositional field. A resolution test is presented in Appendix A, and demonstrates that this grid is sufficient to resolve the diagnostics being studied here. Physical parameters are listed in Tables 1 and 2. The calculation of depth-dependent density, expansivity and diffusivity is detailed in Tackley (1996). Two phase change systems (olivine and pyroxene systems) are treated, with the proportion of each component determined by the local compositional field (Tackley and Xie, 2003). The formulation of density variation due to two phases is detailed in that paper. For the post-perovskite phase transition, the phase boundary is treated as in our previous studies (Nakagawa and Tackley, 2005), in which the phase function method (Christensen and Yuen, 1985) is used. Phase change parameters are listed in Table 2. Fig. 1 shows depth profiles of density for the two different mineralogies, with the reference pyroxene profile having a density 3.6% higher than olivine at the CMB. MORB is taken to be 0% olivine, while pyrolite is 60% olivine, so the density contrast between MORB and pyrolite in the CMB region is 2.16% and is roughly constant over the lower mantle, consistent with the most recent high temperature and pressure experiments on MORB (Hirose et al., 2005). Phase change parameters are listed in Table 2.

The initial condition for temperature is adiabatic plus thin thermal boundary layers at top and bottom plus small random perturbations.

Table 2
Physical parameters for multi-component phase changes

Number	Depth (km)	Temperature (K)	$\Delta\rho_{ph}$ (kg m^{-3})	γ (MPa/K)
Olivine–Spinel–Perovskite–post Perovskite				
1	410	1600	280	+2.5
2	660	1900	400	−2.5
3	2700	3000	61.6	+0 or +8
Pyroxene–Garnet–Perovskite–post Perovskite				
1	60	0	350	+0
2	400	1600	100	+1.0
3	720	1900	500	+1.0
4	2700	3000	61.6	+0 or +8

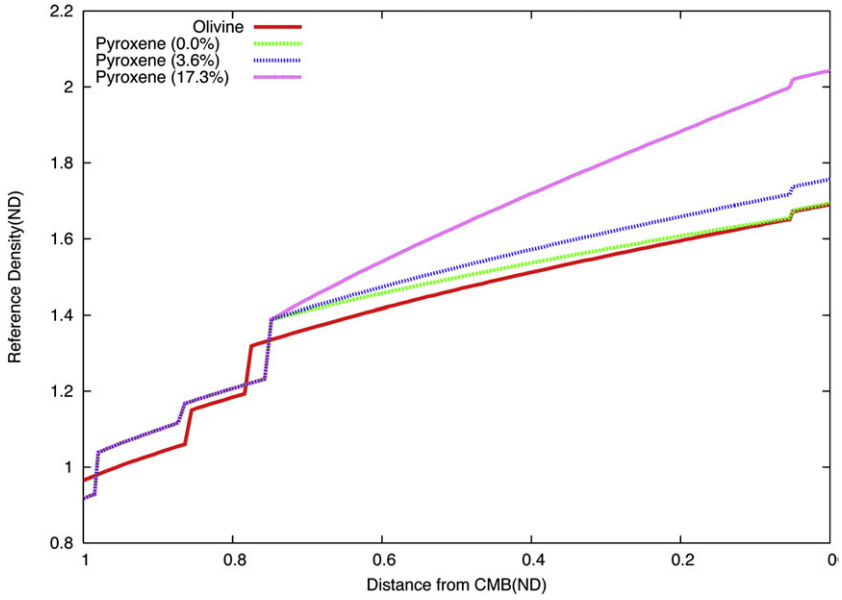

Fig. 1. Reference density profiles for the two phase change systems as a function of non-dimensional distance from the core–mantle boundary.

Composition is initially pyrolitic, except for a thin layer of MORB (thickness 10%=289 km) above the CMB in the thermo-chemical cases. The physical parameters used in this study are listed in Table 1. The averaged internal heating is assumed to be 15.75 non-dimensional (dimensionally 4.3×10^{-12} W/kg) (see Turcotte Schubert, 2001) and is constant with time. The internal heating is 10 times higher in basaltic material (C=1) than in harzburgite (C=0), in order to simulate partitioning of incompatible heat-producing elements into MORB. This results in MORB having a ~3.3 times enhancement of heat production compared to pyrolite. The boundaries are free-slip and isothermal (surface temperature of 300 K and CMB temperature of 4175 K, fixed with time). Cases are run for 20,000 time steps, corresponding to a dimensional time of ~16 billion years using thermal diffusion scaling. The Clapeyron slope (CS) of the post-perovskite phase transition is set to +8 MPa/K, which is close to the value predicted by theoretical estimates (e.g. Oganov and Ono, 2004; Tsuchiya et al., 2004; Wookey et al., 2005).

Seismic anomalies above the CMB are calculated from temperature, composition and phase using

$$\delta \ln V_s = \frac{\partial \ln V_s}{\partial T}\delta T + \frac{\partial \ln V_s}{\partial C}\delta C + \frac{\partial \ln V_s}{\partial X_{\mathrm{ppv}}}\delta X_{\mathrm{ppv}} \tag{3}$$

where δT, δC and δX_{ppv} are anomalies (relative to the mean value) of temperature, composition and phase function at a fixed depth. The scaling coefficients are now discussed. The partial derivative of shear velocity with temperature is assumed to be a quadratic polynomial function of depth fitted to the function calculated by (Trampert et al., 2001; Deschamps et al., 2007), as follows

$$\frac{\partial \ln V_s}{\partial T} = \left(-4.97 + 1.04\times10^{-3}d_0 - 8.01\times10^{-8}d_0^2\right)\times10^{-5} \tag{4}$$

where d is the depth in kilometers. At d_0=2750 km, the depth used here, that partial derivative is -2.71×10^{-5} (K^{-1}). So, for example, a

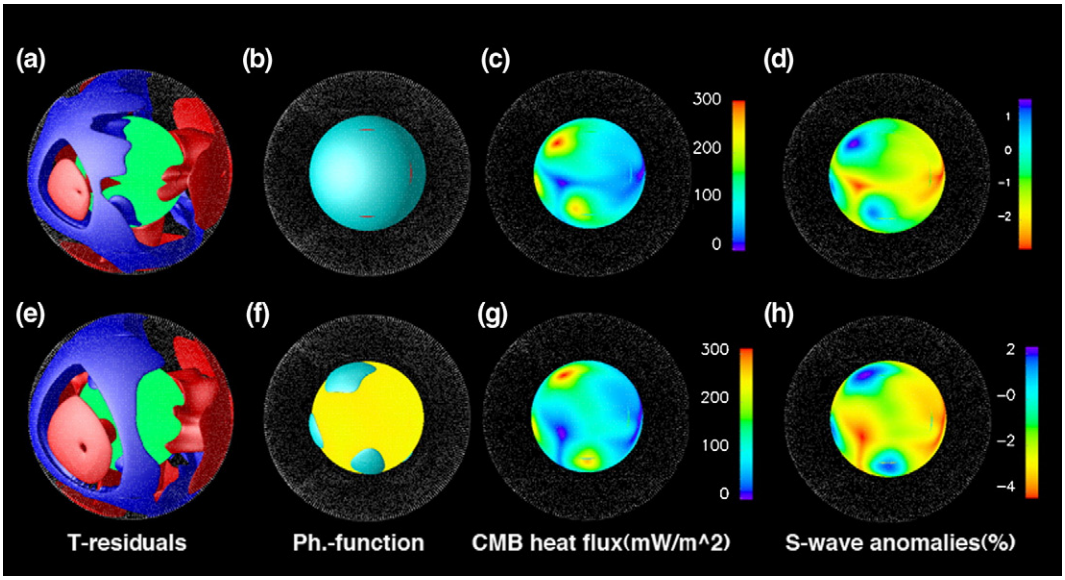

Fig. 2. Isochemical cases at the final time for both Clapeyron slopes ((a)–(d): 0 MPa/K. (e)–(h): +8 MPa/K). (a) and (e) Temperature residuals (red: +250 K from average and blue: −250 K), (b) and (f) Regions containing the post-perovskite phase, (c) and (g) CMB heat flow (color bar is scaled as mW/m^2) and (d) and (h) S-wave anomalies at 2700 km depth. (For interpretation of the references to color in this figure legend, the reader is referred to the web version of this article.)

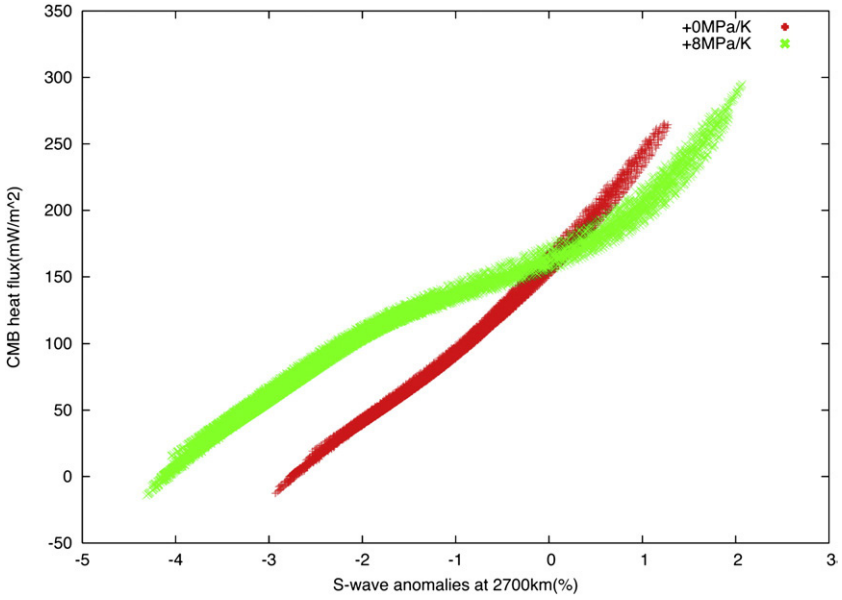

Fig. 3. Scatter plots of CMB heat flux versus S-wave anomaly at 2750 km depth for both isochemical cases. The fit line indicates a least-squares fit for the zero Clapeyron slope case.

temperature anomaly of 1000 K gives a V_s anomaly of −2.71%. For composition, seismic wave velocities for MORB and harzburgite compositions were calculated by J.C. Connolly using free energy minimization to compute the stable mineral assemblages (after Connolly, 2005) and found to be ~2% different, so we here take this coefficient to be 0.02, with the MORB composition being seismically faster. Post-perovskite is assumed to be 2% faster than perovskite, consistent with first principle calculations (Stackhouse et al., 2006; Tsuchiya et al., 2004; Wookey et al., 2005) and with the commonly-observed seismic discontinuity at the top of D" being due to the perovskite to post-perovskite transition.

3. Results

Five cases are presented: two isochemical and three thermo-chemical. The two isochemical cases test the influence of PPV, with one having a zero Clapeyron slope (so that PPV has no influence on lateral variations) and the other having the predicted CS (+8 Ma/K). The composition is fixed at 0.3. In the three thermo-chemical cases, the PPV CS is fixed at the predicted value, but the compressibility of the pyroxene end-member in the lower mantle is varied such that the density contrast between the end-members at the CMB is 0%, 3.6% or 17.3%, where the last value is artificially high in order to enforce a ~flat stable layer.

3.1. Isochemical cases

Fig. 2 shows temperature, phase function, heat flux across the CMB and S-wave anomalies at 2750 km depth for the isochemical cases after 20,000 steps from the initial condition, which corresponds to 16.9 Gyrs using thermal diffusion scaling, or a factor of 3–4 less than this using a surface velocity scaling (see below). The averaged surface heat flow and root-mean-square velocity are 30.1 to 30.4 TW and 0.55 cm/yr, with the latter being a factor of 5–6 lower than Earth's rms. poloidal surface velocity of 3 cm/yr. The thermal structure for these two cases is quite similar, indicating only a small dynamical effect for the PPV transition. Our previous studies also found only a small effect (Nakagawa and Tackley, 2005, 2006; Tackley et al., 2007); the effect is further diminished here by the lower convective vigor, which is known to reduce the dynamical influence of phase transitions (Christensen and Yuen, 1985). As expected, the heat flux is high under downwellings and low under upwellings. Heat flux variations are similar in the two cases but in the case with "predicted" CS the heat flux is noticeably higher underneath cold downwellings where patches of PPV exist (Fig. 2 c and g), perhaps because the downwellings are given a "push" by the PPV transition such that cold material penetrates closer to the CMB. S-wave velocity patterns are also similar but have a higher mean value for the zero CS case because the entire CMB is covered by PPV, which has a 2% higher V_s. In the

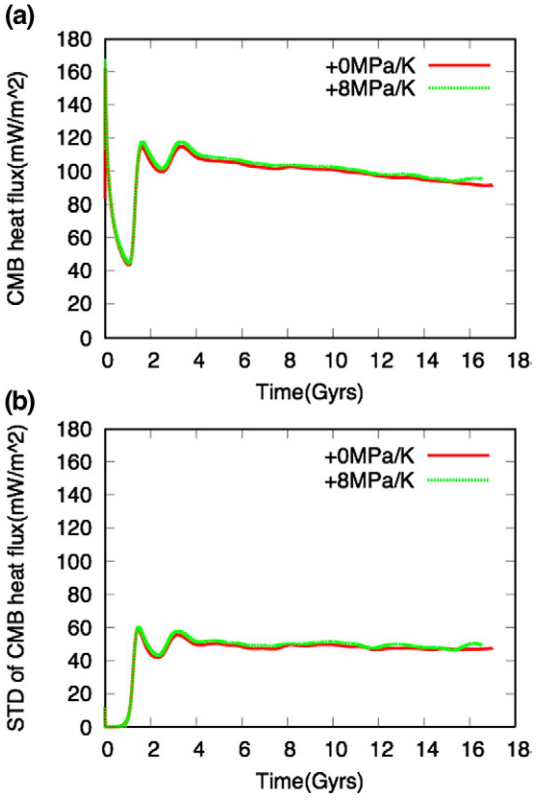

Fig. 4. For the isochemical cases: (a) CMB heat flux, and (b) standard deviation of CMB heat flux variation as a function of time scaled by thermal diffusion time.

Table 3
Summary of results: q_{mean} is a time-averaged CMB heat flux

Case	$q_{peak\text{-}peak}$ (mW/m^2)	q_{std} (mW/m^2)	$\delta V_{spk\text{-}pk}$	q_{mean} (mW/m^2)	q^*
Iso-0PPV	310.8	45.9	4.5%	98.0	1.59
Iso-8PPV	314.6	47.3	6.6%	100.0	1.57
TC-0	218.1	38.6	5.8%	83.9	1.30
TC-3.6	279.4	57.1	7.2%	58.2	2.40
TC-17.3	92.7	15.6	3.4%	24.3	1.91

"predicted" CS case, regions where downwellings reach the CMB region have a V_s that is faster relative to the mean than in the other case, because these cold regions contain patches of PPV. The heat flux and V_s anomalies are highly correlated. The cross-correlation coefficient is 0.993 for the zero CS case and 0.989 for the predicted CS case — slightly lower because the small patches of PPV create a non-linearity in the scaling.

In order to check whether the commonly-assumed linear relationship between CMB heat flux and S-wave velocity is correct, a cloud-cluster analysis is a powerful tool. Fig. 3 shows cloud-cluster (scatter) plots for S-wave anomaly versus CMB heat flux, with each plotted point being one grid cell.

For the zero CS case, which is basically pure thermal convection, there is an almost linear relationship between seismic anomalies and CMB heat flux, but with a notable upward curvature. The reason for this is explored in Appendix B, in which scalings for the δV_s–q_{CMB} relationship are also developed. To summarise, if the temperature profile (with radius) is linear between the CMB and the depth at which anomalies are plotted, then the δV_s–q_{CMB} relationship is also linear. In general, however, a curved temperature profile is expected, for example an error function in the case of a cooling half space (Turcotte and Schubert, 2001). Appendix B shows analytically how this leads to an upward-curved δV_s–q_{CMB} relationship as seen in Fig. 3.

The profile for the predicted CS case displays three trends. At low and high heat flux it parallels the iso-phase case, but at intermediate heat fluxes it is much shallower, transitioning between these two trends. This central section is due to the post-perovskite phase transition, which is here taken to have a 2% S-wave change that is spread out using a tanh function in temperature (and pressure) space. Appendix B shows how this profile can be well fit by adding an extra term that takes into account the PPV transition.

Again, because high heat flux regions occupy only a small fraction of the CMB surface area, this non-linearity has only a small effect on the correlation coefficient, but it would have important implications for the estimation of the heat flux anomalies of individual features: they would be overpredicted by the linear least-squares fit. If PPV covered a larger fraction of the CMB, then the correlation coefficient would likely be lower.

To study the relationship between heat flux variations and mean heat flux, Fig. 4 shows the time evolution of mean CMB heat flux and standard deviation of lateral variations in CMB heat flux, i.e.,

$$q_{std} = \frac{1}{S}\int_S \left(q_{CMB}(\theta,\varphi) - \langle q_{CMB}(\theta,\varphi)\rangle\right)^2 dS \quad (6)$$

where a value of $<q_{CMB}(\theta, \phi)>$ indicates averaged CMB heat flux over the entire CMB surface. These graphs are almost the same for the two cases. The CMB heat flux (Fig. 4 b) changes slowly and has a final value of 91.6 mW/m^2 for the zero CS case and 95.2 mW/m^2 for the predicted CS case. These correspond to a global CMB heat flow of about 14.5 TW — within the current range of estimates and lower than in our initial cylindrical-geometry PPV study (Nakagawa and Tackley, 2004) because that study did not include internal heating. q_{CMB} decreases very slowly with time – about 15% in the last 12 billion years, which is due to the mantle slowly heating up – by ~100 K in the same time period. This is so slow, however, that it is not expected to affect the diagnostics analysed here. The standard deviation of lateral variations of q_{CMB} (Fig. 4 b and Table 3) is a factor of ~two lower at 45.9–47.3 mW/m^2 for the two cases, indicating that regions of extremely high or low heat flux occupy only a small fraction of the CMB surface area. The peak-to-peak heat flux heterogeneity is around 310 to 314 mW/m^2 (see Table 3). In order to clarify these points, Fig. 5 shows histograms of CMB heat flux for the two isochemical cases. The final averaged q_{CMB} is consistent with the peak in the histograms, but the distribution is asymmetric about this mean value, with a long tail at high heat flux values. The heat flux ratio $q^*=(q_{max}-q_{min})/(2q_{ave})$ (Olson and Christensen, 2002) (right column of Table 3) is ~1.57–1.59 at the end of calculation, meaning that half the peak-to-peak variation is comparable to or larger than the mean value. According to geodynamo simulations (Olson and Christensen, 2002; Christensen and Olson, 2003), dynamo processes fail for heat flux ratios q^* equal to or larger than about 1, so no dynamo would exist for the heat flux ratios of >=1 predicted here, a point that is discussed further later.

3.2. Thermo-chemical cases

Fig. 6 shows the temperature residuals, compositional isosurfaces, PPV phase regions, CMB heat flux and S-wave anomalies at 2750 km depth and after 20,000 timesteps from the initial condition for the three different deep mantle density differences as discussed earlier and plotted in Fig. 1. With 0% density variation (Fig. 5 b) the initial dense layering has been completely swept up by the convection. For a 3.6% density variation (2.16% between MORB and pyrolite), the dense MORB material is swept into ridge-shaped piles that are anticorrelated with the locations of post-perovskite material (Fig. 5 g and h), and some of it is entrained into the convective flow. For a 17.3% density

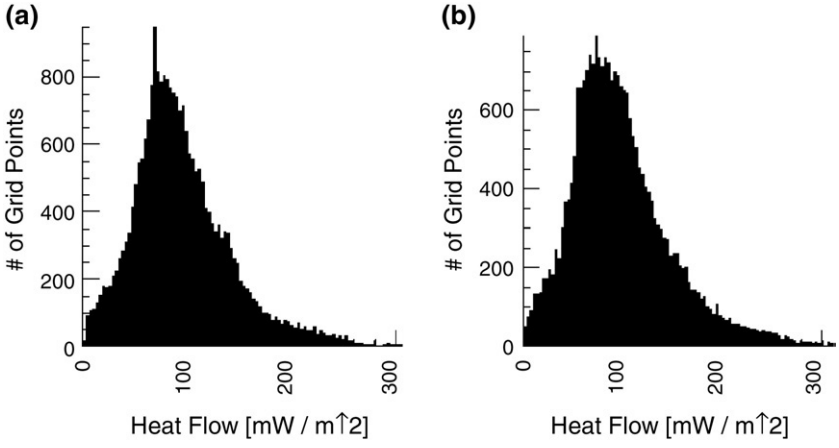

Fig. 5. Histograms of CMB heat flux for two isochemical cases; (a) 0 MPa/K and (b) +8 MPa/K for pPv phase transition.

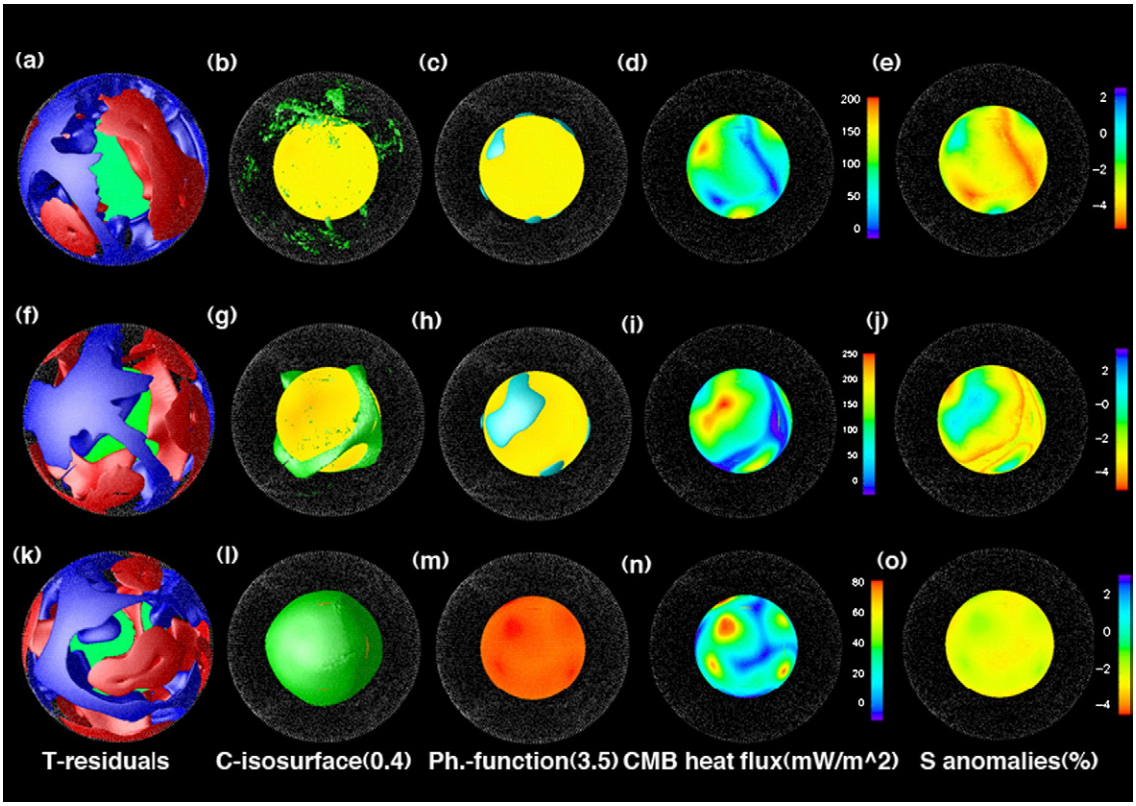

Fig. 6. Thermo-chemical cases at the final time. (a)–(e) 0% density difference at CMB, (f)–(j) 3.6% density difference at CMB, and (k)–(o) 17.3% density difference at CMB. Color bar for CMB heat flux is in mW/m^2.

variation (10.4% between MORB and pyrolite), the global layer remains and undulates slightly (Fig. 5 l). For this case, there is no post-perovskite phase (Fig. 5 m) because the dense layer raises the temperature in the CMB region such that it is always higher than phase boundary between perovskite and post-perovskite, somewhat similar to previous 3-D cartesian box cases (Nakagawa and Tackley, 2006). Note that in the simulations in this paper, the CMB temperature (4177 K) is higher than the temperature of the PPV phase boundary at the CMB (4021 K), so that the CMB is in the perovskite stability field and either a double crossing or no crossing of the PPV boundary is obtained, as explained by (Hernlund et al., 2005). The existence of the lower crossing back to perovskite is being increasingly reinforced by seismological results (Hernlund et al., 2005; Lay et al., 2006; van der Hilst et al., 2007).

Whereas the CMB heat flow variations (Fig. 6 d,i,n) reflect the locations of upwellings and downwellings, the V_s anomalies (Fig. 6 e,j,o)

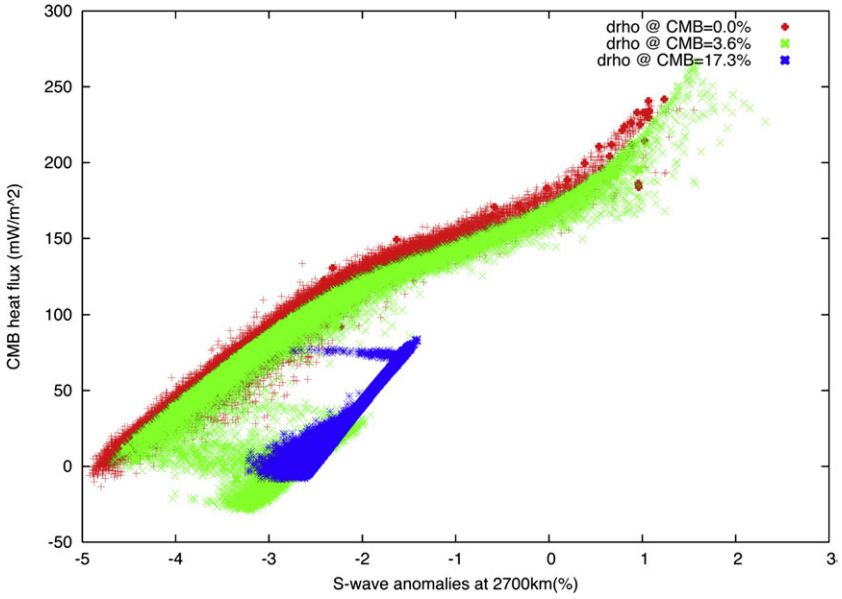

Fig. 7. Scatter plots for all thermo-chemical cases.

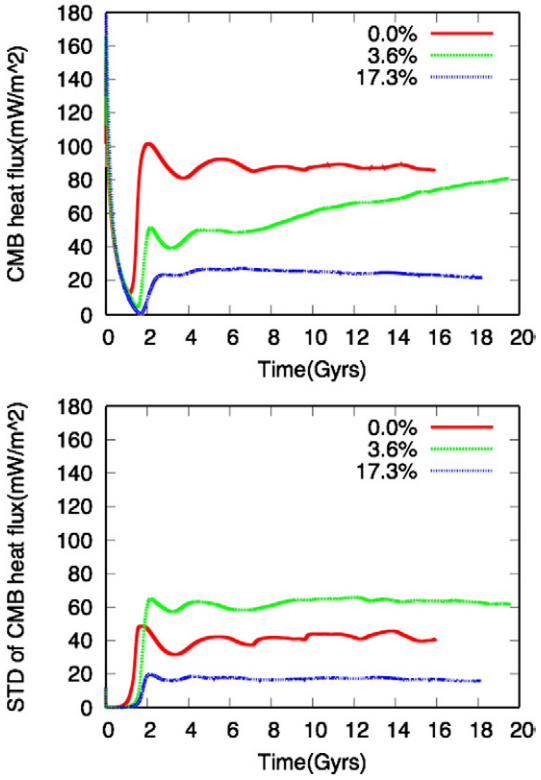

Fig. 8. For the thermo-chemical cases: (a) CMB heat flux and (b) standard deviation of CMB heat flux as a function of time.

display a more complex pattern because of the additional influence of PPV and dense crust. PPV acts to amplify the high δV_s in cold regions as with the isothermal results. Dense crust at the CMB is swept under upwellings thus acts to increase V_s in regions where it is normally low (slow). Nevertheless, because regions of PPV and dense crust are localized, the cross-correlation coefficients between CMB heat flux and V_s anomalies are still relatively high: 0.978 for 0%, 0.790 for 3.6% and 0.963 for 17.3%. Interestingly, for the case with 3.6% density difference at the CMB (Fig. 5 j), rim-like regions at the edges of dense piles are the slowest regions. This feature is similar to tomographic images obtained by various techniques to resolve the structure in the CMB region (Ni et al., 2002; To et al., 2005) and does not correspond to any feature observed in CMB heat flow. Generally, extremely low S-wave anomalies correspond to extremely low heat flux but, in such sharp-edged regions, the correlation is lost because of the effect of composition on V_s: the region with the lowest heat flux does not have the lowest V_s. Other than that, large-scale heat flux and V_s structures in the 3.6% case appear to be well-correlated.

These points become clearer in the q_{CMB} vs. δV_s scatter plots (Fig. 7). The 0% density contrast case (red) is very similar to the isochemical + PPV case, with a region of low $\delta q/\delta V_s$ in the middle of the curve that is caused by the PPV transition. The 3.6% density contrast case is also similar but has an additional branch at low q_{CMB}. This additional branch is associated with dense subducted MORB in the ridge-shaped piles above the CMB, which is assumed to be 2% faster than regular material, but has a similar temperature to the hottest regular material. Appendix B gives an analytical fit for this additional branch. This leads to a non-uniqueness such that in a certain range of δV_s there are two possible values of q_{CMB}, and in a certain range of q_{CMB} there are two possible values of δV_s.

In the extreme density variation case all points are in the MORB branch, because the entire CMB is covered with a layer of MORB that extends above the observation depth. There is also a much smaller range of q_{CMB} and δV_s values than in the cases with no layer or an intermittent layer, because the dense layer prevents cold slabs from reaching this depth and has a relatively small range of temperature variations: it is relatively hot causing the high q_{CMB} and δV_s values.

Fig. 8 shows the time evolution of CMB heat flux and of the standard deviation of lateral variations in CMB heat flux. The standard deviation of q_{CMB} is quite different between the different cases. It is small for the extreme density case because the CMB is blanketed by a layer of dense material, and in this simulation it appears that heat transport through the layer is mainly by conduction (Fig. 8 b). The reference $\Delta\rho$ case has the largest standard deviation in q_{CMB}, because of the low q_{CMB} underneath the dense piles. The final heat flux for all cases shown in Table 3 is around 85.2 mW/m^2 for 0%, 79.9 mW/m^2 for 3.6% case, and 24.7 W/m^2 for the 17.3% case. The peak-to-peak lateral CMB heat flux variation is around 218 to 279 mW/m^2 but 92 mW/m^2 for the 17.3% case (Table 3).

Histograms of CMB heat flux (Fig. 9) again indicate a consistency between the most probable values and the mean q_{CMB} (Table 3). The standard deviations range from 15.6 to 57.1 mW/m^2. In the completely layered case, the peak value is much lower than in the 0 density contrast case. The 3.6% density contrast case has two peaks, with the lower one corresponding to inside the dense piles; indeed, it looks like a combination of the 0% and 17.3% cases. The heat flux ratio q^* is between 1.30 and 2.40 (right column of Table 3). This range is also high compared to what geodynamo simulations find is the maximum that can still permit a geodynamo to operate.

4. Summary and discussion

In this study, numerical simulations of thermo-chemical, multi-phase, compressible convection in a 3-D spherical shell have been

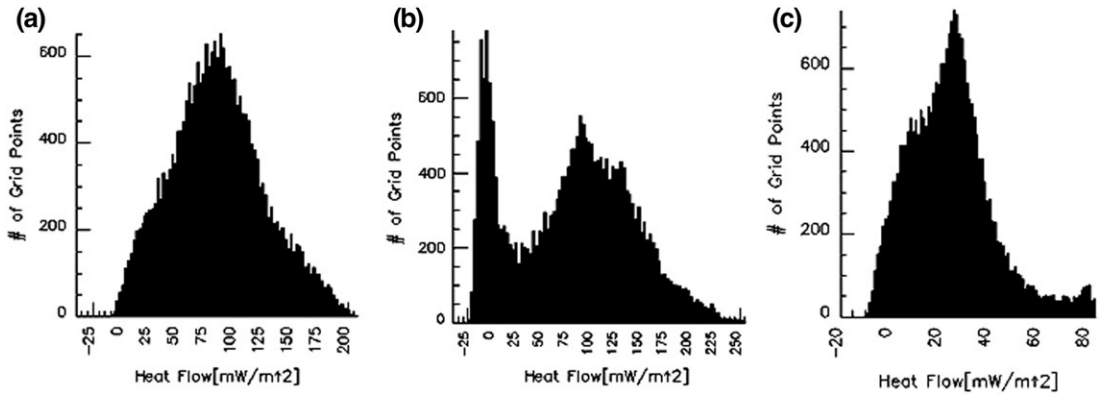

Fig. 9. Histograms of CMB heat flux for all thermo-chemical cases. (a) 0.0%, (b) 3.6% and (c) 17.3% density difference.

used to investigate how variations in CMB heat flux (q_{CMB}) and seismic shear wave velocity anomaly (δV_s) are influenced by the post-perovskite phase transition and compositional layering above the CMB (complete or partial), and thus whether heat flux variations can be straightforwardly inferred from variations in V_s. The results of the numerical simulations are well fit using analytical scalings presented in Appendix B. The main findings are:

(1) A linear scaling between δV_s and q_{CMB} is a good approximation only in cases with no compositional variations and no PPV, although it will slightly underestimate the heat flux in regions with the highest δV_s. due to the upwards curvature of the δV_s–q_{CMB} trend.
(2) Lateral variations in the occurrence of PPV create a non-linear relationship between δV_s and q_{CMB}. Because PPV occurs in cold regions and it has a higher V_s than perovskite, it amplifies the high δV_s in these regions, reducing the slope of the dq_{CMB}/dV_s line. The relationship is still unique, and we have obtained a suitable functional form (Appendix B).
(3) If subducted MORB (or other anomalously dense material) exists in some regions above the CMB (e.g., as piles) then it generates a non-linear and possibly non-unique relationship between δV_s and q_{CMB}. Dense material gets swept under hot upwellings, which normally have negative δV_s. If MORB is seismically fast, as assumed here, then it reduces the slow anomalies under upwellings and generates a non-uniqueness in the δV_s and q_{CMB} relationship. Piles of hot dense material are then surrounded by a ring of low δV_s.
(4) In isochemical convection cases q_{CMB} ranges from slightly above zero to somewhat more than twice the average heat flux, so that the heat flux ratio q^* is greater than or of order 1, although the probability distribution is asymmetric with a longer tail at high q_{CMB} values. Compositionally-dense piles can induce negative heat flux under themselves (i.e., into the core), which can lead to larger q^*.
(5) If compositionally-dense material covers the entire CMB then it greatly reduces the range of δV_s and q_{CMB}, although not q^* because the average F_{CMB} is also reduced.

In all five cases, $q^* \geq 1$, which means that the peak-to-peak amplitude of lateral heat flux variations is at least twice the mean heat flux. A global compositional layer certainly reduces variations in q_{CMB}, but it also reduces the mean value, so q^* is similar. This is potentially problematic because in geodynamo simulations (e.g., Olson and Christensen, 2002; Christensen and Olson, 2003), such large values tend to cause dynamo action to shut off. This is, apparently, due to the low q_{CMB} regions, under which stable stratification can exist in the core (e.g., Olson and Christensen, 2002). Therefore what matters is not the absolute peak-to-peak range, but the minimum values, and the results presented here show that the q_{CMB} probability distribution tends to be asymmetric, with a long tail at the high q_{CMB} end. Minimum q_{CMB} values are around zero for isochemical convection, but can become negative underneath piles of dense material, if they exist. One potentially important factor is that most dynamo models have been run with parameters (Rayleigh number, Ekman number, high magnetic Prandtl number) that are far from realistic for Earth's core, and with parameters that are closer to Earth-like, larger variations in q_{CMB} might be tolerated (D. Gubbins, personal communication). Successful solutions with $q^*=0.9$ have already been obtained by (Gubbins et al., 2007). Another possibility is that a global melt layer just above the CMB might act to even out heat flux (Labrosse et al., 2007).

The presented mantle models will be improved and extended in several ways in the future, to check the robustness of these findings. The convective vigor could be brought closer to Earth-like (requiring higher resolution). Viscosity variation with temperature could be increased to a more realistic value, which would influence small-scale convection and plume formation in the CMB region. Plate-like behavior and differentiation due to melting (to self-consistently generate compositional variations) could be included, as in previous models. The models could simultaneously address coupled core–mantle evolution by including decaying heat sources and a cooling core, as with previous models.

There are some uncertainties in the scalings between temperature, composition, phase and V_s in the deep mantle that might affect the results. Recent measurements of δV_s for postperovskite (Murakami et al., 2007) suggest that it is smaller than assumed, at 0.5% rather than 2%, in which case the non-linearity in the scalings found here would be reduced. These authors attribute the extra 1.5% δV_s of the "Lay" discontinuity (Lay and Helmberger, 1983) to anisotropy of PPV, which, if included here, would further complicate the interpretation of δV_s in terms of q_{CMB}. The composition-dependence of V_s is also somewhat uncertain. If MORB were seismically slow (instead of fast) then the non-uniqueness in the δV_s–q_{CMB} mapping could be removed.

Finally it is noted that core–mantle thermal coupling appears to be an important influence on the dynamo and that computing heat flux variations from seismic wave velocities leads to a magnetic field that has several features observed on Earth, as indicated by the recent modelling of (Gubbins et al., 2007).

Acknowledgements

TN was financially supported by Grants-in-aid for Scientific research (for young scientist category B) allocated from Ministry of Education, Culture, Sports, Science and Technology (MEXT) of Japan. Supported for computational resources by research institute for information technology, Kyushu University (TN). The authors also thank Mark Jellinek and two anonymous reviewers for constructive reviews, and James Connolly for providing us with calculations of MORB and pyrolite seismic wave velocity.

Appendix A. Resolution test

In order to check that the used resolution of 64×192×64×2 cells is sufficient to resolve the features that we study here, we compare results from one case, the isochemical case with the post-perovskite transition, with those of an identical case with twice the resolution in each direction, i.e., 128×384×128×2 cells. A comparison of thermal structure is shown in Fig. A1, the time-dependence of thermal diagnostics is shown in Fig. A2 and a δV_s–q_{CMB} scatter plot in Fig. A3. The characteristic features of the thermal structures are quite similar although different in detail because of different initial random perturbations. There are only minor differences in time averaged diagnostics (heat flux and standard deviation of lateral variations in CMB heat flow). The scatter plot for the high-resolution case almost completely overlies the scatter plot for the standard resolution case, except for some minor deviation at the high heat flux end, which does not affect the arguments or analytical trend

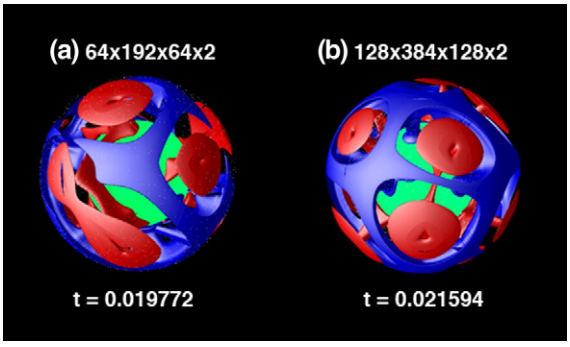

Fig. A1. Temperature residual for standard resolution and double resolution cases.

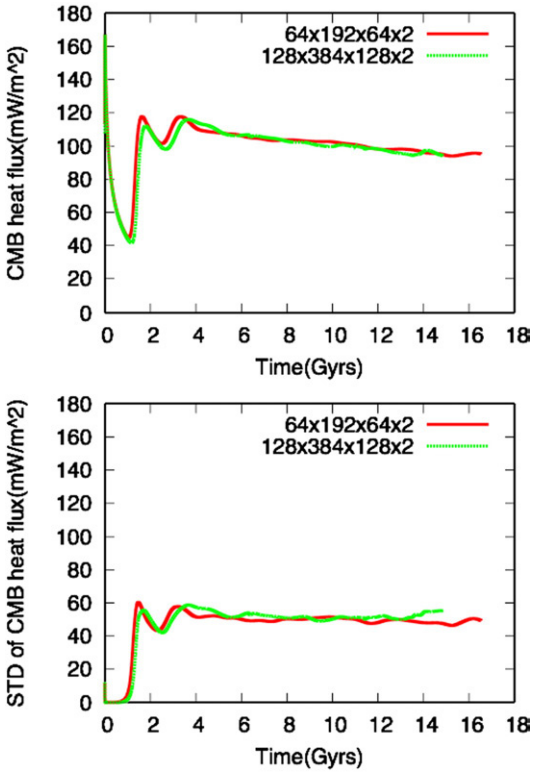

Fig. A2. Thermal diagnostics as a function time for standard and double resolution cases: (a) surface heat flux, (b) CMB heat flux and (c) standard deviation CMB heat flux.

developed here. Therefore the resolution used in this paper (64×192×64×2) is sufficient for the analysis being performed.

Appendix B. Analytical scaling for V_s versus heat flux relationship

Here, a scaling is developed to explain the relationship between S-wave velocity anomaly a fixed distance above the CMB and heat flux across the CMB. It is developed in stages: first, assuming that the temperature profile is linear with radius; second, assuming a more realistic error function temperature profile, and finally, adding the effects of post-perovskite and compositional variations.

Linear temperature profile

Assuming a linear temperature profile that varies laterally, the heat flux q at a point on the CMB and the temperature T a distance h above that point can be written:

$$q = -k\left(\frac{\partial T}{\partial r}\right); \quad T = T_c - h\left(\frac{\partial T}{\partial r}\right) \tag{B1}$$

where k is thermal conductivity, r is radius, and T_c is the CMB temperature. Assuming that the temperature gradient varies laterally and a constant scaling coefficient $\partial \ln V_s/\partial T$ between V_s and T, q and V_s can be related:

$$\frac{\partial q}{\partial \ln V_s} = -\frac{k}{h}\Big/\left(\frac{\partial \ln V_s}{\partial T}\right) \tag{B2}$$

which predicts the q–δV_s gradient observed in Figs. 3 and 7. Making a quantitative comparison, the parameters in the numerical simulations are $k = 15.93\ \mathrm{Wm^{-1}\ K^{-1}}$, $h = 133$ km, $\partial \ln V_s/\partial T = -2.72\times10^{-5}\ \mathrm{K^{-1}}$, leading to $\partial q/\partial \ln V_s = 4.42\ \mathrm{W\,m^{-2}}$ per 100% change in V_s, or $44.2\ \mathrm{mW\,m^{-2}}$/%. This slope is similar to the low heat flux end of the curves in Figs. 3 and 7, at which one would expect the temperature profile to be approximately linear. This linear prediction is plotted as the green line in Fig. B1a.

Error function temperature profile

In general the temperature profile is expected to be curved. An error function profile is expected for a cooling half space (Turcotte and Schubert, 2001) and we here use it as a first approximation. Assuming an error function profile leads to the possibility of a curved q–δV_s relationship. The temperature at height h and corresponding heat flux are:

$$T = T_c - \Delta T erf\left(\frac{h}{d}\right); \quad q = k\left(\frac{\partial T}{\partial r}\right)_{rcmb} = -\frac{2}{\sqrt{\pi}}\frac{k\Delta T}{d} \tag{B3}$$

where ΔT is the temperature difference across the lower thermal boundary layer and d is its thickness (at 84% of the temperature

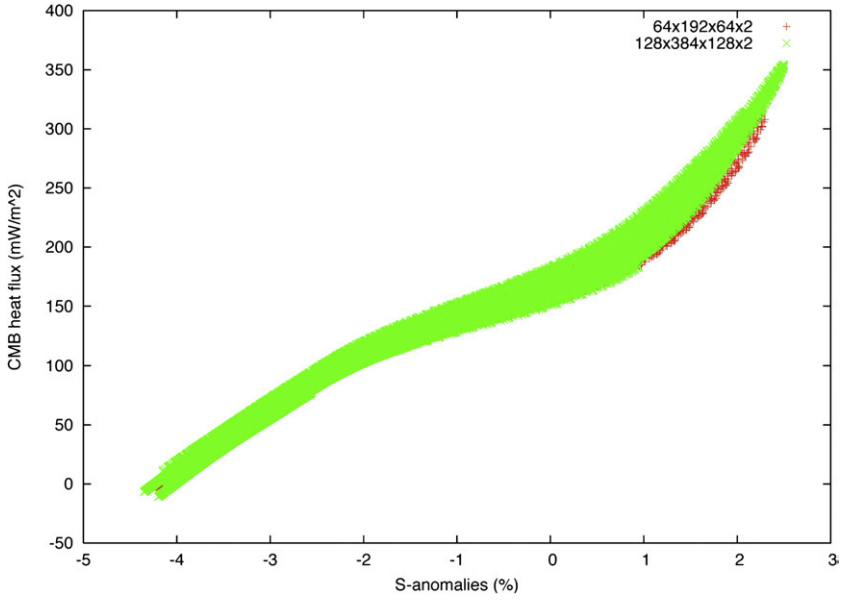

Fig. A3. Scatter plot comparing double resolution with standard resolution.

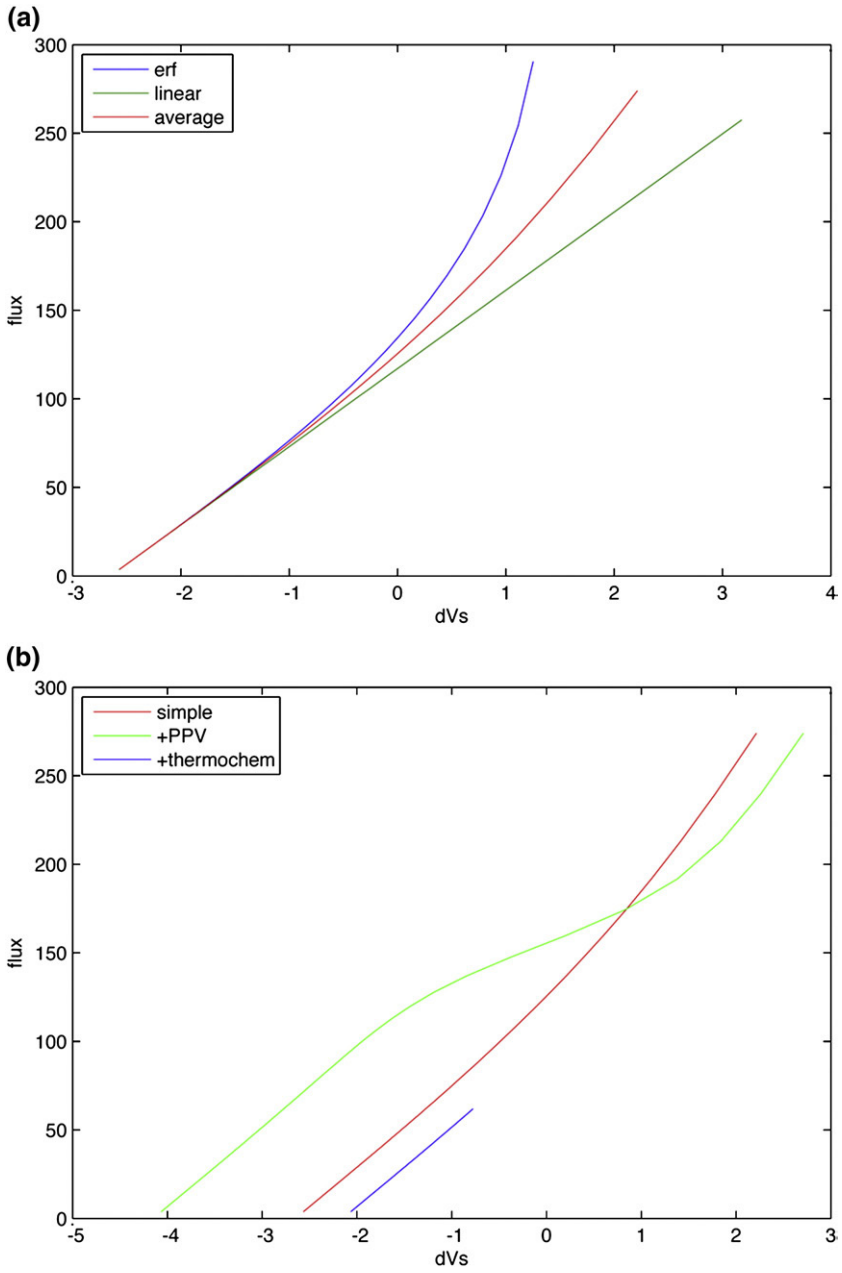

Fig. B1. Analytical relationship between heat flux across the CMB and seismic anomalies 140 km above the CMB. (a) Temperature effects only, with three different assumptions about the temperature profile in the deep mantle: linear (green), error function (blue), the average of these (red). (b) Temperature (red), temperature + post-perovskite (green) and temperature + post-perovskite + dense layer (blue), all with the 'average' temperature profile. (For interpretation of the references to color in this figure legend, the reader is referred to the web version of this article.)

drop). Assuming that ΔT is fixed but d varies laterally, the latter relationship can be rearranged to give d as a function of q:

$$d = -\frac{2}{\sqrt{\pi}}\frac{k\Delta T}{q} \tag{B4}$$

which allows d to be eliminated:

$$T = T_c - \Delta T erf\left(\frac{h\sqrt{\pi}}{2k\Delta T}q\right) \tag{B5}$$

leading to an equation relating S-wave velocity anomaly to q:

$$\delta \ln V_S = -\Delta T\left(\frac{\partial \ln V_S}{\partial T}\right) erf\left(\frac{h\sqrt{\pi}}{2k\Delta T}q\right) + C. \tag{B6}$$

Assuming $\Delta T = 1500$ K and h = 133 km, q is plotted against δV_s in Fig. B1 (blue curve). At low heat flux, the temperature profile is approximately linear over a distance h above the CMB, leading to a linear q-V_s relationship, but at high heat flux the curvature of the temperature profile becomes important, leading to a curvature of the q–δV_s relationship. The actual curves in Fig. 3 and 7 appear intermediate between this error function prediction (blue), and that from the linear assumption above (green). This implies that the actual temperature profile is intermediate between linear and error function, and/or that ΔT varies laterally as well. Therefore, as a first approximation, to fit the numerical experiments we take the average of the linear and error function models, i.e.,

$$T_{avg} = \frac{1}{2}\left(T_{linear} + T_{erf}\right);\ \ q_{avg} = \frac{1}{2}\left(q_{linear} + q_{erf}\right). \tag{B7}$$

This average fit is shown as the red curve in Fig. B1a, and compares well with the isochemical, isophase case shown in Fig. 3.

Post-perovskite

Post-perovskite is assumed to be 2% faster than perovskite. At a fixed depth, corresponding approximately to a fixed pressure, this transition occurs at a particular temperature, but is spread out numerically using a tanh function, so occurs over some temperature range. A term can be added to account for this:

$$\delta \ln V_{ppv} = \delta \ln V_{avg} - 0.02\left[\frac{1}{2}\left\{\tanh\left(\frac{T-3000}{200}\right)-1\right\}\right] - 0.015 \qquad \text{(B8)}$$

where the last term is an arbitrary offset that is here set in order to be similar to that in the numerical results. This is compared to the isophase 'average' fit in Fig. B1b, and fits quite well the numerical results plotted in Figs. 3 and 7.

Compositional variations

Material in dense piles is assumed to be 2% faster than regular material at the same temperature, so we can simply write that:

$$\delta V_{dense} = \delta V_{ppv} + 0.02. \qquad \text{(B9)}$$

The dense material is hot, so this branch appears at the low heat flux end of the curve. The possible existence of both compositions with the same temperature leads to two parallel branches that causes a non-uniqueness in the F-V_s relationship. This branch is plotted in Fig. B1b.

This simple argument does not take into account the different internal heating rate in the dense material, which would be expected to make the MORB branch more concentrated towards low q and low V_s. The good fit of our scaling, however, suggests that this is a second order effect. Overall, Fig. B1b matches well Figs. 3 and 7, indicating that the analytic scaling developed above is reasonable.

References

Aubert, J., Amit, H., Hulot, G., 2007. Detecting thermal boundary control in surface flows from numerical dynamos. Phys. Earth Planet. Inter. 160, 143–156.

Bloxham, J., 2000a. Sensitivity of the geomagnetic axial dipole to thermal core–mantle interactions. Nature 405, 63–65.

Bloxham, J., 2000b. The effect of thermal core–mantle interactions on the paleomagnetic secular variation. Phil. Trans. R. Soc. Lond. A. 358, 1171–1179.

Bloxham, J., Gubbins, D., 1987. Thermal core–mantle interactions. Nature 325, 511–513.

Christensen, U.R., Olson, P., 2003. Secular variation in numerical geodynamo models with lateral variations of boundary heat flow. Phys. Earth Planet. Int. 138, 39–54.

Christensen, U.R., Yuen, D.A., 1985. Layered convection induced by phase transitions. J. Geophys. Res. 90, 10291–10300.

Clement, B.M., 1991. Geographical distribution of transitional VGPs: evidence for non-zonal equatorial symmetry during the Matsuyama–Brunhes geomagnetic reversal. Earth Planet. Sci. Lett. 104, 48–58.

Connolly, J.A.D., 2005. Computation of phase equilibria by linear programming: a tool for geodynamic modeling and its implication to subduction zone decarbonation. Earth Planet. Sci. Lett. 236, 524–541.

Costin, S.O., Buffett, B.A., 2004. Preferred reversal paths caused by a heterogeneous conducting layer at the base of mantle. J. Geophys. Res. 109, B06101. doi:10.1029/2003JB002853.

Deschamps, F., Trampert, J., Tackley, P.J., 2007. Thermo-chemical structure of the lower mantle: seismological evidence and consequences for geodynamics, in Superplume: Beyond Plate Tectonics. In: Yuen, D.A., et al. (Ed.), Springer, pp. 293–320.

Glatzmaier, G.A., Coe, R.S., Hongre, L., Roberts, P.H., 1999. The role of the Earth's mantle in controlling the frequency of geomagnetic reversals. Nature 401, 885–890.

Gubbins, D., Willis, A.P., Sreenivasan, B., 2007. Correlation of Earth's magnetic field with lower mantle thermal and seismic structure. Phys. Earth Planet. Int. 162, 256–260.

Hernlund, J.W., Thomas, C., Tackley, P.J., 2005. A doubling of the post-perovskite phase boundary and structure of the Earth's lowermost mantle. Nature 434, 882–886.

Hirose, K., Takafuji, N., Sata, N., Ohishi, Y., 2005. Phase transition and density of subducted MORB crust in the lower mantle. Earth Planet. Sci. Lett. 237, 239–251.

Kageyama, A., Sato, T., 2004. The 'yin–yang grid': an overset grid in spherical geometry. Geochem. Geophys. Geosyst. Q09005. doi:10.1029/2004GC000734.

Kageyama, A., 2005. Dissection of a sphere and yin–yang grids. J. Earth Simulator 3, 20–28.

Labrosse, S., Hernlund, J.W., Coltice, N., 2007. A crystallizing dense magma ocean at the base of the Earth's mantle. Nature 450, 866–869.

Laj, C.A., Mazaud, A., Weeks, M., Fuller, M., Herrero-Bervera, E., 1991. Geomagnetic reversal paths. Nature 351, 447.

Larson, R.L., Olson, P., 1991. Mantle plumes control magnetic reversal frequency. Earth Planet. Sci. Lett. 107, 437–447.

Lay, T., Helmberger, D.V., 1983. A shear velocity discontinuity in the lower mantle. Geophys. Res. Lett. 10, 63–66.

Lay, T., Hernlund, J., Garnero, E.J., Thorne, M.S., 2006. A post-perovskite lens and D" heat flux beneath the central Pacific. Science 314, 1272–1276.

Love, J.J., 2000. Statistical assessment of preferred transitional VGP longitudes based on paleomagnetic lava data. Geophys. J. Int. 140, 211–221.

McNamara, A.K., Zhong, S., 2004. Thermochemical structures within a spherical mantle: superplumes or piles? J. Geophys. Res. 109, B07402. doi:10.1029/2003JB002847.

McNamara, A.K., Zhong, S., 2005. Thermochemical structures beneath Africa and the Pacific Ocean. Nature 437, 1136–1139.

Murakami, M., Hirose, K., Sata, N., Ohishi, Y., Kawamura, K., 2004. Phase transition of $MgSiO_3$ perovskite in the deep lower mantle. Science 855–858.

Murakami, M., Sinogeikin, S.V., Bass, J.D., Sata, N., Ohishi, Y., Hirose, K., 2007. Sound velocity of $MgSiO_3$ post-perovskite phase: a constraint on the D" discontinuity. Earth Planet. Sci. Lett. 259, 18–23.

Nakagawa, T., Tackley, P.J., 2004. Effects of the post-perovskite phase change in compressible mantle convection. Geophys. Res. Lett. 31, L16611. doi:10.1029/GL020648.

Nakagawa, T., Tackley, P.J., 2005. Deep mantle heat flow and thermal evolution of the Earth's core in thermochemical multiphase models of mantle convection. Geochem. Geophys. Geosyst. 6, Q08003. doi:10.1029/2005GC000967.

Nakagawa, T., Tackley, P.J., 2006. Three-dimensional structures and dynamics in the deep mantle: effects of post-perovskite phase change and deep mantle layering. Geophys. Res. Lett. 33, L21S11. doi:10.1029/2006GL025719.

Ni, S., Tan, E., Gurnis, M., Helmburger, D.V., 2002. Sharp sides to the African super plume. Science 296, 1850–1852.

Oganov, A.R., Ono, S., 2004. Theoretical and experimental evidence for a post-perovskite phase of $MgSiO_3$ in Earth's D" layer. Nature 430, 445–448.

Oldham, D., Davies, J.H., 2004. Numerical investigation of layered convection in a three-dimensional shell with application to planetary mantles. Geochem. Geophys. Geosyst. 5, G12C04. doi:10.1029/2003GC000603.

Olson, P., Christensen, U.R., 2002. The time-averaged magnetic field in numerical dynamos with non-uniform boundary heat flux. Geophys. J. Int. 151, 809–823.

Olson, P., Glatzmaier, G.A., 1996. Magnetoconvection and thermal coupling of the Earth's core and mantle. Phil, Trans. R. Soc. Lond. A. 354, 1413–1424.

Ritsema, J., McNamara, A.K., Bull, A.L., 2007. Tomographics filtering of geodynamic models: implications for model interpretation and large-scale mantle structure. J. Geophys. Res. 112, B01303. doi:10.1029/2006JB004566.

Stackhouse, S., Brodholt, J.P., Price, G.D., 2006. Elastic anisotropy of $FeSiO_3$ end-member of the perovskite and post-perovskite phases. Geophys. Res. Lett. 33, L01304. doi:10.1029/2005GL023887.

Stemmer, K., Harder, H., Hansen, U., 2006. A new method to simulate convection strongly temperature- and pressure-dependent viscosity in a spherical shell: applications to the Earth's mantle. Phys. Earth Planet. Int. 157, 223–249.

Tackley, P.J., 1993. Effects of strongly variable viscosity on time-dependent, three-dimensional models of mantle convection. Geophys. Res. Lett. 20, 2187–2190.

Tackley, P.J., 1996. Effects of strongly variable viscosity on three-dimensional compressible convection in planetary mantles. J. Geophys. Res. 101, 3311–3332.

Tackley, P.J., 1998. Three-dimensional simulations of mantle convection with a thermo-chemical basal boundary layer: D"? In: Gurnis, M., et al. (Ed.), The Core-Mantle Boundary Region. American Geophysical Union, Washington D.C., pp. 231–253.

Tackley, P.J., Xie, S., 2003. STAG3D: a code for modeling thermo-chemical multiphase convection in Earth's mantle. Second MIT Conference on Computational Fluid and Solid Mechanics.

Tackley, P.J., Stevenson, D.J., Glatzmaier, G.A., Schubert, G., 1993. Effects of an endothermic phase transition at 670 km depth in a spherical model of convection in the Earth's mantle. Nature 361, 699–704.

Tackley, P.J., Nakagawa, T., Hernlund, J.W., 2007. Influence of the post-perovskite transition on thermal and thermo-chemical mantle convection, in AGU Geophysical Monograph on "The Last Phase Transition". In: Hirose, K., Brodholt, J., Lay, T., Yuen, D.A. (Eds.), pp. 229–247.

To, A., Romanowicz, B., Capdeville, Y., Takeuchi, N., 2005. 3D effects of sharp boundaries at the borders of the African and Pacific superplumes: observation and modeling. Earth Planet. Sci. Lett. 233, 137–153.

Trampert, J., Vacher, P., Vlaar, N., 2001. Sensitivities of seismic velocities to temperature, pressure and composition in the lower mantle. Phys. Earth Planet. Int. 124, 255–267.

Tsuchiya, T., Tsuchiya, J., Umemoto, K., Wentzcovitch, R.M., 2004. Phase transition in $MgSiO_3$ perovskite in the Earth's lower mantle. Earth Planet. Sci. Lett. 224, 241–248.

Turcotte, D.L., Schubert, G., 2001. Geodynamics, Second Edition. Cambridge. 456pp.

van der Hilst, R.D., de Hoop, M.V., Wang, P., Shim, S.H., Ma, P., Tenorio, L., 2007. Seismostratigraphy and thermal structure of Earth's core–mantle boundary region. Science 315, 1813–1817.

Wookey, J., Stackhouse, S., Kendall, J.-M., Brodholt, J., Price, G.D., 2005. Efficacy of the post-perovskite phase as an explanation for lowermost mantle seismic properties. Nature 438, 1004–1007.